Nanoscale

PAPER

View Article Online
View Journal

Cite this: DOI: 10.1039/d6nr00658b

Top-down and bottom-up reconstruction of matter in charged water microdroplets

Prakrati Patidar,[a] Anubhav Mahapatra,[a] Bhagyashri Soni,[a] Soham Chowdhury,[a] Sujan Manna,[a] Amoghavarsha Ramachandra Kini,[a] Anirban Som,[a] Depanjan Sarkar*[a,b] and Thalappil Pradeep*[a,b,c]

Received 14th February 2026,
Accepted 6th April 2026

DOI: 10.1039/d6nr00658b

rsc.li/nanoscale

The synthesis of metal nanoparticles is conventionally achieved either by top-down fragmentation of bulk metals by mechanical milling or by bottom-up chemical reduction of metal salts, with each route typically relying on specific methods, distinct infrastructure, and conditions. In this work, we show that charged water microdroplets provide a unified platform that supports both pathways, and the results are presented for noble metals. Micron-sized powders of silver and copper undergo efficient top-down fragmentation in charged microdroplets, yielding stable crystalline nanoparticles under mild, reagent-free conditions, whereas gold powder remains largely resistant to fragmentation under identical electrospray parameters. In parallel, bottom-up electrospray of acetate solutions of silver, copper, and gold generates nanoparticles of all three metals *via* reduction and nucleation within the same microdroplet environment. The contrasting top-down responses of Ag and Cu *versus* Au, together with the universal bottom-up formation for all of them, reveal a metal-dependent fragmentation behaviour that is independent of initial particle morphology, yet governed by intrinsic material properties. These results establish charged water microdroplets as a versatile, green, and scalable medium in which complementary top-down and bottom-up mechanisms for noble metal nanoparticle formation coexist, expanding the scope of microdroplet chemistry in nanomaterial synthesis.

Introduction

Microdroplets have recently emerged as powerful miniature reactors that can accelerate reactions and enable transformations that are difficult or impossible in bulk solutions.[1–6] Their high surface-to-volume ratios, steep interfacial gradients, and intense local electric fields create unique reaction environments, often enabling rapid, selective chemistry under ambient, green conditions.[3,7,8] Charged water microdroplets have attracted particular attention as a simple yet versatile platform for materials synthesis for various applications.[9–13]

Our group has been pioneering the bottom-up synthesis of nanomaterials in charged microdroplets.[14–21] We have shown that diverse nanomaterials, including bimetallic nanostructures, 1D nanowires and nanorods, 2D nanosheets, and 3D noble–metal and metal–oxide architectures, can be generated directly from precursor salt solutions by electrospraying under ambient conditions, without added surfactants, reducing agents, or external heating.[9,15–17] In these systems, rapid evaporation and extreme charge densities drive nucleation and growth, establishing charged microdroplets as a general and sustainable platform for bottom-up nanomaterial formation. More recently, our research group demonstrated that charged water microdroplets can induce top-down fragmentation of hard natural minerals, such as quartz and ruby, producing nanoparticles under apparently mild conditions.[1] These reports suggest that microdroplets can mediate not only solution-phase chemistry but also mechanically and electrostatically driven disintegration of solids, although both have not been demonstrated together across the same chemical systems.

Noble metal nanoparticles composed of silver, gold, and copper are central to catalysis,[22] sensing, plasmonics, and energy technologies, and are typically prepared either by bottom-up reduction of metal salts in solution or by top-down fragmentation of bulk metals using methods such as mechanical milling, laser ablation, or sputtering.[23–25] These routes offer complementary advantages, synthetic control *versus* surfactant-free purity, but usually rely on distinct energy-consuming equipment and operating conditions. Despite the rapid

[a]*DST Unit of Nanoscience (DST UNS) & Thematic Unit of Excellence (TUE), Department of Chemistry, Indian Institute of Technology Madras (IITM), Chennai 600036, India. E-mail: depanjan_coe@icsrpis.iitm.ac.in, pradeep@iitm.ac.in*
[b]*Centre of Excellence on Molecular Materials and Functions, Department of Chemistry, Indian Institute of Technology Madras (IITM), Chennai 600036, India*
[c]*International Centre for Clean Water, IIT Madras Research Park, 2nd Floor, B-Block, Kanagam Road, Taramani, Chennai 600113, India*

growth of microdroplet chemistry, it remains unclear whether a single charged microdroplet platform can support both bottom-up synthesis from dissolved noble metal ions and top-down fragmentation of metallic solids, and how intrinsic material properties govern these two different pathways.

In this communication, we address this question by investigating micron-sized powders and acetate salts of Ag, Cu, and Au in charged water microdroplets. We show that the same electrospray conditions that drive universal bottom-up nanoparticle formation from dissolved noble metal precursors also induce efficient top-down fragmentation of silver and copper powders, although gold resists breakup and largely preserves its parent morphology. By comparing these metal-dependent top-down responses with the universal bottom-up behaviour, we establish charged microdroplets as a unified, green platform for creating complementary pathways to noble metal nanoparticles.

Results and discussion

Top-down meets bottom up

The two experimental configurations explored in this work are summarized schematically in Fig. 1. In the top-down mode, suspensions of micron-sized metal powders were electrosprayed, and any reduction in feature size was studied by analyzing deposited films. In the bottom-up mode, metal acetate solutions were electrosprayed under identical conditions to probe nanoparticle formation from dissolved precursors. A detailed experimental procedure is presented in the experimental section (SI) (Fig. 1).

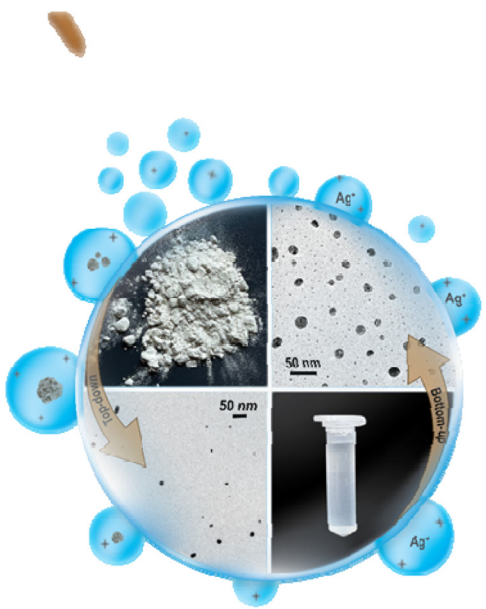

Fig. 1 Schematic showing the top-down breakdown of bulk metal powders into nanoparticles and the bottom-up synthesis of metal nanoparticles from metal salt solutions in charged microdroplets. Representative images of the precursors and corresponding TEM images of the deposited nanoparticles are included to illustrate the two electrospray methods.

Top-down fragmentation of silver

Top-down fragmentation was first investigated using suspensions of micron-sized silver powder in water. The parent material, as observed by field emission scanning electron microscopy (FESEM), exhibited particles in the micron-size range (4–7 μm) with irregular morphology (Fig. 2A). After electrospray deposition of the suspension at an applied potential of 2.5 kV with a tip-to-substrate distance of 2 cm, this bulk morphology was not retained. Instead, large-area transmission electron microscopy (TEM) images revealed a dense distribution of nanoparticles (NPs) across the grid, indicating that fragmentation into NPs had occurred within the charged microdroplets (Fig. 2B). The crystalline nature of these particles was confirmed by high-resolution transmission electron microscopy (HRTEM), which showed lattice fringes with d = 0.23 nm corresponding to the (111) plane of face-centred cubic Ag (Fig. 2C). Transmission electron microscopy-energy dispersive spectroscopy (TEM-EDS) mapping revealed that the particles were silver (Fig. 2D). The UV-visible spectrum of the electrospray-deposited material suspended in water exhibited a plasmonic absorption band at ~400 nm, characteristic of Ag NPs. X-ray photoelectron spectroscopy (XPS) analysis of the Ag 3d region showed peaks at 368.0 and 374.0 eV, corresponding to Ag $3d_{5/2}$ and Ag $3d_{3/2}$ of metallic silver (Fig. 2E). After characterizing the NPs, their plasmonic activity was evaluated. Surface-enhanced Raman spectroscopy (SERS) measurements showed an enhancement of 10^4 in Raman intensity, consistent with plasmonically active Ag NPs, when methylene blue (10 μM) was used as a probe molecule (Fig. 2F).

Morphology-independent fragmentation of silver powders

To assess the influence of the initial morphology, silver flakes with a thin sheet-like structure were examined under otherwise identical conditions. Although the parent material displayed a markedly different morphology under FESEM (Fig. S1A), electrospray deposition again led to the formation of NPs, as observed in large-area TEM images (Fig. S1B). HRTEM confirmed the crystalline nature of these particles (Fig. S1C). NP formation during electrospray is therefore concluded to be largely independent of the starting morphology of the silver powder, suggesting that interfacial stresses and electric-field-driven forces in the droplet dominate over the initial shape of the solid, in determining the outcome.

Top-down fragmentation of copper

Copper powders were studied in an analogous manner. The parent copper material consisted of nearly spherical micron-sized (≤10 μm) particles (Fig. 3A). Following electrospray deposition, TEM imaging revealed a uniform distribution of Cu NPs on the grid (Fig. 3B). HRTEM images showed lattice fringes with d = 0.208 nm, corresponding to the (111) plane of face-centred cubic copper (Fig. 3C). TEM-EDS mapping con-

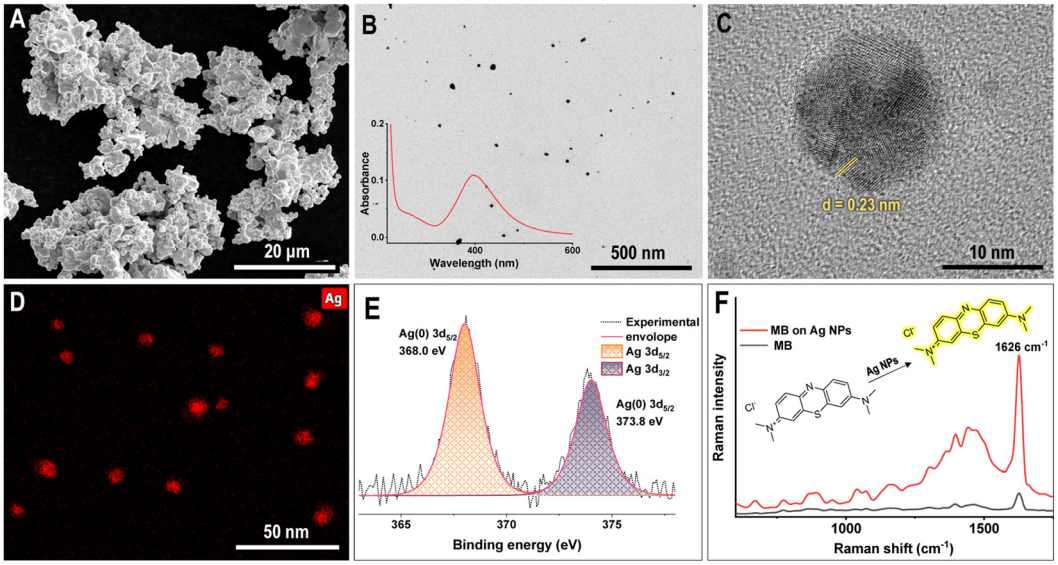

Fig. 2 Experimental data corresponding to the top-down approach for silver. (A) FESEM image of the parent silver powder. (B) Low-magnification TEM image showing a large-area distribution of Ag nanoparticles formed by electrospray and the corresponding UV-visible spectrum of the Ag nanoparticles. (C) HRTEM image of an Ag nanoparticle exhibiting multiple lattice fringes (only d = 0.23 nm corresponding to the (111) is labelled) corresponding to face-centred cubic Ag. (D) TEM-EDS elemental mapping of Ag. (E) XPS spectrum of Ag nanoparticles showing the Ag 3d core-level peaks, confirming the metallic state of silver. (F) SERS spectra of Ag nanoparticles formed by electrospray, showing enhanced Raman signals for methylene blue (MB) as a substrate.

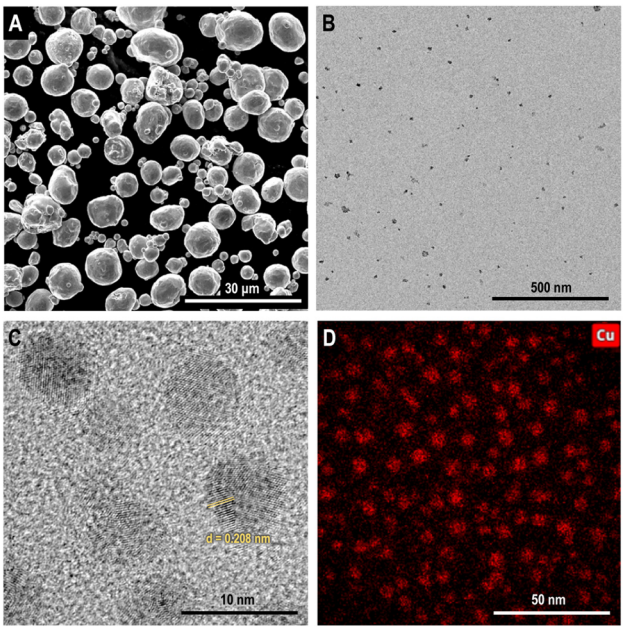

Fig. 3 Experimental data corresponding to the top-down approach for copper. (A) FESEM image of the parent copper powder. (B) Low-magnification TEM image showing a large-area distribution of Cu nanoparticles formed by electrospray. (C) HRTEM image of Cu nanoparticles exhibiting multiple lattice fringes (only d = 0.208 nm corresponding to the (111) plane of face-centred cubic Cu is labelled). (D) TEM-EDS elemental mapping of the formed Cu nanoparticles.

firmed that the NPs were composed of copper (Fig. 3D). XPS spectra of the deposited material, collected after longer deposition times to ensure sufficient signal, displayed a main Cu $2p_{3/2}$ feature at about 932.1 eV, assigned to Cu(0), together with a peak at 934.3 eV attributed to Cu(II), which is ascribed to partial surface oxidation during deposition and subsequent air exposure (Fig. S2). These observations indicate that, as with silver, micron-sized copper powders undergo effective fragmentation into crystalline NPs in charged water microdroplets under mild, reagent-free conditions.

Voltage-dependent Cu particle disintegration

To investigate the role of applied potential in microdroplet-mediated nanoparticle formation, we conducted additional experiments at 0 V (50 psi N2 gas for nebulization) and at voltages ranging from 1.5 to 4 kV. At zero voltage, larger Cu particles (~200 nm to a few microns) were observed, reflecting purely mechanical nebulization driven by gas pressure. With increasing voltage, particle size progressively decreased (down to ~1–2 nm at 4 kV), due to enhanced electric field-driven disintegration at the air–water interface (Fig. S3). These results confirm the critical synergy between electric fields and microdroplet dynamics, providing deeper mechanistic insight into the voltage-dependent milling efficiency.

Resistance of gold to fragmentation

The same top-down protocol was then applied to gold powders. FESEM analysis of the parent Au sample revealed a heterogeneous mixture of rods, triangular plates, hexagons, spheres, and other faceted structures (Fig. 4A). In contrast to Ag and Cu, electrospray deposition did not result in extensive NP formation. TEM images of the deposited material showed that the parent morphology was largely preserved, and only a few isolated NPs (highlighted with a black circle in Fig. 4B)

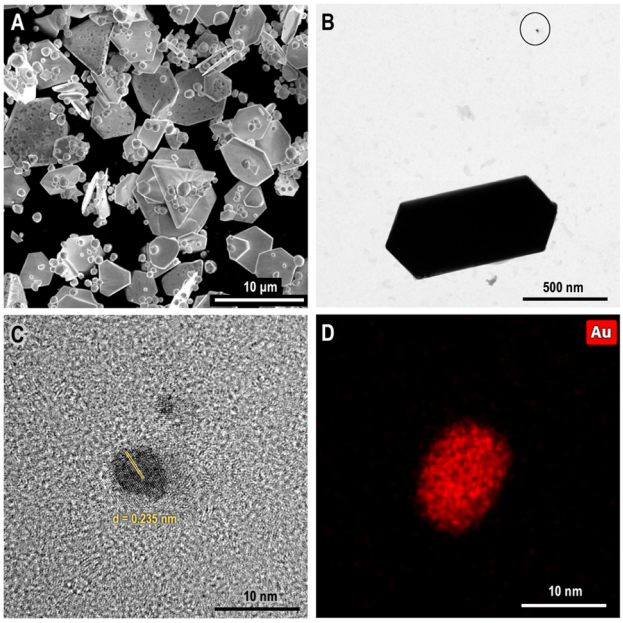

Fig. 4 Experimental data corresponding to the top-down approach for gold. (A) HRSEM image of the parent gold powder. (B) Low-magnification TEM image of the deposited material. (C) HRTEM image of an Au nanoparticle exhibiting multiple lattice fringes (only d = 0.235 nm corresponding to the (111) corresponding to face-centred cubic Au is labelled). (D) TEM-EDS elemental mapping of Au.

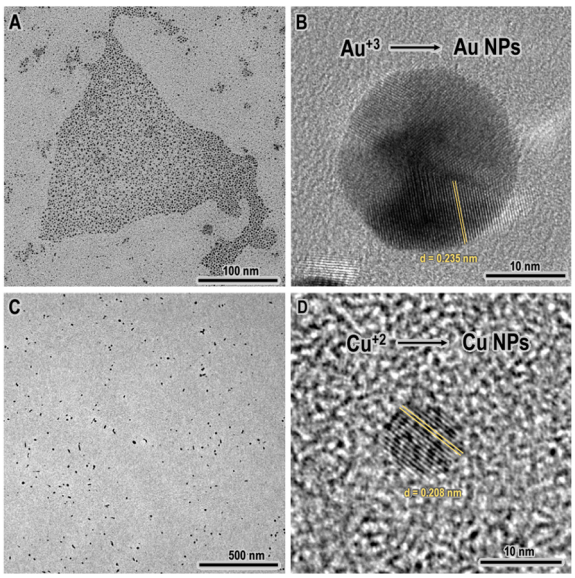

Fig. 5 TEM images of nanoparticles formed by the bottom-up route in charged microdroplets. (A) Low-magnification TEM image of Au nanoparticles. (B) HRTEM image of an Au nanoparticle exhibiting lattice fringes with an interplanar spacing of d = 0.235 nm, corresponding to the (111) plane of face-centred cubic Au. (C) Low-magnification TEM image of Cu nanoparticles. (D) HRTEM image of a Cu nanoparticle exhibiting lattice fringes with an interplanar spacing of d = 0.208 nm, corresponding to the (111) plane of face-centred cubic Cu.

were observed across the grid (Fig. 4B). HRTEM analysis of these NPs confirmed their crystalline nature, with lattice fringes of d = 0.235 nm corresponding to the (111) plane of gold (Fig. 4C). TEM-EDS mapping verified the presence of Au in these particles (Fig. 4D). Variation in the applied potential and tip-to-substrate distance did not result in a significant increase in NP yield. Under the conditions investigated, gold is therefore concluded to be resistant to fragmentation in charged microdroplets, in sharp contrast to silver and copper.

Bottom-up nanoparticle formation from metal acetates

To examine the corresponding bottom-up pathway under identical microdroplet conditions, acetate solutions of Ag, Cu, and Au were electrosprayed. In all three cases, NP formation was observed: Ag NPs are shown on the 'bottom-up' part of Fig. 1, while TEM and HRTEM images for copper and gold (Fig. 5) confirm crystalline NPs with lattice fringes corresponding to the (111) planes of fcc Cu and Au. NPs were obtained without added surfactants, reducing agents, or external heating. These results show that in contrast to the selective top-down behavior, bottom-up NP formation from metal acetate precursors occurs for all three noble metals under the same charged microdroplet conditions. Thus, rapid solvent evaporation, high local charge densities, and interfacial redox processes in the microdroplets provide a general driving force for nucleation and growth of noble metal NPs, starting from dissolved ions.

Mechanistic considerations for microdroplet-mediated milling

Charged water microdroplets generate extreme local stresses through multiple synergistic mechanisms that collectively overcome the metal's mechanical strength. The disintegration process involves both physical forces from electric fields and droplet dynamics, amplified by chemically reactive interfacial conditions. These factors are discussed in the following two paragraphs.

Interfacial electric fields and mechanochemical stresses in charged microdroplets

Under the present electrospray conditions (applied potential of 2–2.5 kV, 1.5–2 cm tip-to-substrate distance, flow rate 0.1 mL h^{-1}), the primary water microdroplets are expected to reach radii of tens of micrometres at the emitter, followed by repeated Rayleigh fission, ultimately generating submicrometre progeny droplets with surface charge densities approaching the Rayleigh limit. Under this scenario, two major forces act on the particles within the droplets. First, for such tiny, charged droplets, surface electric fields are in the range of 10^7–10^9 V cm^{-1}, consistent with recent charge–dynamics measurements and simulations.[26,27] A conservative interfacial field for droplets of radius (r) in the range of 50–500 nm yields a Maxwell electrostatic stress (approximated using the formula $\sigma_M = 1/2\xi_0 E^2$) of 4.4 MPa to 44.3 GPa (for E = 10^7 and E = 10^9 V cm^{-1}, respectively), acting normal to the liquid–solid interface, comparable to typical yield stresses of noble metals (20–200 MPa, depending on processing) in their

bulk form. We have taken the vacuum permittivity ξ_0, to be 8.85×10^{-12} C^2 N^{-1} m^{-2}. Second, the curvature of submicrometre–nanometer-sized water droplets gives Laplace pressures, $\Delta P = 2Y/r$ in the order of 0.28 MPa to 2.8 MPa (for r = 500 and 50 nm, respectively), consistent with simulations.[28] The combined action of these electrostatic and Laplace pressures, applied dynamically during repeated droplet impact and deformation in anisotropic droplets, provides mechanochemical driving force to nucleate and propagate interfacial defects leading to particle disintegration. In our experiments, this manifests as the transformation of 5–10 μm Ag and Cu powders into dense distributions of 5–20 nm crystalline nanoparticles across the TEM grid, under ambient conditions, a degree of size reduction that would otherwise require far more energetic top-down methods. Our voltage-dependent particle disintegration experiments (Fig. S3) further support these mechanistic insights, showing larger Cu particles at 0 V and progressive size reduction with increasing voltage up to 4 kV.

Ion/proton-induced chemical stress

While these electrostatic and capillary forces act on the metal–water interface, they are not sufficient to fragment the metal particles solely by mechanical stress during such short droplet-particle contact times; selective breakup instead requires concurrent chemical weakening of the lattice. At the surface of charged water microdroplets, over the course of flight, the preferential orientation of solvent (water in this case) and interfacial charge separation enrich protons (H^+) and other ionic species, creating a localized acidic, highly oxidizing environment that is far more reactive than the bulk.[29] Under such conditions, field-assisted protonation and interfacial redox reactions at the metal surface can generate transient $Ag^+/Cu^+/Cu^{2+}$ species together with thin, defective oxide/hydroxide layers, introducing local volume mismatch and chemical strain at grain boundaries and pre-existing defect sites. This chemically induced strain, along with Maxwell and Laplace stresses, promotes fragmentation at weakened interfaces, making crack initiation and growth of nanoscale fragments upon rapid solvent evaporation. The efficient conversion of micron-sized Ag and Cu powders into 5–20 nm particles within 30 min is consistent with such a synergistic mechanochemical–chemical fragmentation pathway, in which interfacial reactions both soften the lattice and continuously regenerate fresh reactive surfaces. This phenomenon correlates with the mineral fragmentation observed earlier.[1]

Metal-dependent resistance of gold to fragmentation

In contrast to Ag and Cu, gold remains largely resistant to microdroplet-mediated milling under the same electrospray conditions, underscoring the importance of intrinsic material properties in governing fragmentation. Its higher cohesive strength and greater chemical inertness resist both oxide formation and interfacial weakening, so that the combined Maxwell and Laplace stresses, even together with interfacial protonation and redox, are insufficient to drive extensive cracking and particle breakup within the short flight time of our experiments. Experimentally, this is reflected in the parent rods, plates, and faceted Au particles being retained with only sparse 10–20 nm Au nanoparticles observed, in sharp contrast to the near-complete conversion of 5–10 μm Ag and Cu powders into dense populations of 5–20 nm particles. Taken together, these observations suggest that while mechanochemical and ion/proton-induced chemical stresses operate generically in charged microdroplets, efficient fragmentation is realized only for metals that are both mechanically and chemically labile (Ag, Cu), whereas Au remains below this threshold under the same conditions.

Overall, these results show that charged water microdroplets provide a single reaction environment in which two complementary routes to noble metal nanoparticles operate. In the top-down mode, micron-sized Ag and Cu powders fragment into crystalline nanoparticles in a morphology-independent but metal-dependent manner, whereas Au remains essentially intact. In the bottom-up mode, acetate solutions of Ag, Cu, and Au all yield nanoparticles under identical ambient electrospray conditions, establishing charged microdroplets as a common, green platform for both fragmentation and synthesis of noble metal nanostructures.

Conclusions

In conclusion, we demonstrate that charged water microdroplets function as a unified, green platform that accesses both top-down and bottom-up pathways to noble metal nanoparticles under identical ambient electrospray conditions. In a single configuration, micron-sized powders of Ag and Cu are fragmented into crystalline nanoparticles in a metal-dependent yet morphology-independent manner, while Au remains essentially intact, revealing that microdroplet-mediated fragmentation is controlled primarily by intrinsic material properties rather than by starting particle shape. In parallel, acetate solutions of Ag, Cu, and Au yield nanoparticles in all cases without added surfactants, reducing agents, or external heating, demonstrating a general bottom-up route from dissolved precursors within the same microdroplet environment. By combining selective top-down breakup with universal bottom-up synthesis, this work establishes charged microdroplets as a simple, reagent-efficient, and intrinsically selective medium for the production of noble metal nanoparticles, opening opportunities for metal-specific manipulation, separation, and scalable nanomaterial synthesis on a common ambient platform.

Author contributions

P. P. data collection, data analysis, data interpretation, and writing the manuscript. A. M., Electrospray, SEM imaging, B. S., electrospray, S. C., XPS measurement, S. M., Raman measurement, A. K., XPS analysis, A. S., TEM measurements, D. S. conception and design of work, supervision of data col-

lection and analysis, interpretation of results, drafting and editing of the article. T. P. conception and design of work, supervision of data analysis, interpretation of results, writing and editing of the final version of the article.

Conflicts of interest

There are no conflicts to declare.

Data availability

The data supporting this article are included in the main article and its supplementary information (SI). Supplementary information is available. See DOI: https://doi.org/10.1039/d6nr00658b.

No additional data have been deposited in external repositories.

Acknowledgements

We acknowledge the ANRF Science and Engineering Research Board (SERB), the Department of Science and Technology (DST), and the Government of India for their research funding. T. P. acknowledges the financial support of SERB through the SUPRA scheme: SPR/2021/000439. We acknowledge the support of the Centre of Excellence on Molecular Materials and Functions under the institution of Eminence scheme of IIT Madras. TEM measurements were performed at the ANRF SERB National Facility for Cryo-Electron Microscopy, IIT Madras.

References

1 B. K. Spoorthi, K. Debnath, P. Basuri, A. Nagar, U. V. Waghmare and T. Pradeep, *Science*, 2024, **384**, 1012–1017.
2 X. Yan, R. M. Bain and R. G. Cooks, *Angew. Chem., Int. Ed.*, 2016, **55**, 12960–12972.
3 K. R. Wilson and A. M. Prophet, *Annu. Rev. Phys. Chem.*, 2024, **75**, 185–208.
4 Z. Wei, Y. Li, R. G. Cooks and X. Yan, *Annu. Rev. Phys. Chem.*, 2020, **71**, 31–51.
5 J. K. Lee, S. Banerjee, H. G. Nam and R. N. Zare, *Q. Rev. Biophys.*, 2015, **48**, 437–444.
6 T. Pradeep, *ACS Sustainable Chem. Eng.*, 2026, **14**, 25–30.
7 G. Rovelli, M. I. Jacobs, M. D. Willis, R. J. Rapf, A. M. Prophet and K. R. Wilson, *Chem. Sci.*, 2020, **11**, 13026–13043.
8 P. Basuri, A. Chakraborty, T. Ahuja, B. Mondal, J. S. Kumar and T. Pradeep, *Chem. Sci.*, 2022, **13**, 13321–13329.
9 D. Sarkar, M. K. Mahitha, A. Som, A. Li, M. Wleklinski, R. G. Cooks and T. Pradeep, *Adv. Mater.*, 2016, **28**, 2223–2228.
10 Q. Lu, B. Sanogo, T. Kumar, B. Bin Xu and X. Zhang, *Adv. Mater.*, 2025, **37**, e09486.
11 A. Li, Z. Baird, S. Bag, D. Sarkar, A. Prabhath, T. Pradeep and R. G. Cooks, *Angew. Chem., Int. Ed.*, 2014, **53**, 12528–12532.
12 D. Sarkar, A. Mahapatra, A. Som, R. Kumar, A. Nagar, A. Baidya and T. Pradeep, *Adv. Mater. Interfaces*, 2018, **5**, 1800667.
13 D. Sarkar, B. Mondal, A. Som, S. J. Ravindran, S. K. Jana, C. K. Manju and T. Pradeep, *Glob. Chall.*, 2018, **2**, 1800052.
14 K. S. Aswathi, K. Unni, S. Mukhopadhyay, A. Som, S. Chowdhury, S. K. Jana, D. Sarkar and T. Pradeep, *Nanoscale Horiz.*, 2026, **11**, 1053–1062.
15 K. Unni, J. S. Kumar, A. Som, D. Sarkar and T. Pradeep, *ACS Sustainable Chem. Eng.*, 2024, **12**, 11957–11967.
16 D. Sarkar, A. Som, K. Unni, S. Manna and P. Thalappil, *Small*, 2024, **21**, 2400159.
17 A. Jana, S. K. Jana, D. Sarkar, T. Ahuja, P. Basuri, B. Mondal, S. Bose, J. Ghosh and T. Pradeep, *J. Mater. Chem. A*, 2019, **7**, 6387–6394.
18 D. Sarkar, R. Singh, A. Som, C. K. Manju, M. A. Ganayee, R. Adhikari and T. Pradeep, *J. Phys. Chem. C*, 2018, **122**, 17777–17783.
19 D. Satyabola, T. Ahuja, S. Bose, B. Mondal, P. Srikrishnarka, M. P. Kannan, B. K. Spoorthi and T. Pradeep, *J. Phys. Chem. C*, 2021, **125**, 10998–11006.
20 D. Sarkar, A. Som and T. Pradeep, *Anal. Chem.*, 2017, **89**, 11378–11382.
21 A. Som, D. Sarkar, S. Kanhirathingal and T. Pradeep, *Part. Part. Syst. Charact.*, 2017, **34**, 1700101.
22 M. B. Gawande, A. Goswami, F.-X. Felpin, T. Asefa, X. Huang, R. Silva, X. Zou, R. Zboril and R. S. Varma, *Chem. Rev.*, 2016, **116**, 3722–3811.
23 G. Habibullah, J. Viktorova and T. Ruml, *Nanoscale Res. Lett.*, 2021, **16**, 47.
24 N. Baig, I. Kammakakam and W. Falath, *Mater. Adv.*, 2021, **2**, 1821–1871.
25 T. K. Sau and A. L. Rogach, *Adv. Mater.*, 2010, **22**, 1781–1804.
26 H. Hao, I. Leven and T. Head-Gordon, *Nat. Commun.*, 2022, **13**, 280.
27 H. Xiong, J. K. Lee, R. N. Zare and W. Min, *J. Phys. Chem. Lett.*, 2020, **11**, 7423–7428.
28 S. M. A. Malek, F. Sciortino, P. H. Poole and I. Saika-Voivod, *J. Phys.: Condens. Matter*, 2018, **30**, 144005.
29 X. Jia, J. Wu and F. Wang, *JACS Au*, 2024, **4**, 4141–4147.

